LASER & PHOTONICS REVIEWS
www.lpr-journal.org

Ultra-Sparse Aperiodic Silicon Optical Phased Array Using High-Performance Thermo-Optic Phase Shifter

*Huaqing Qiu, Yong Liu, Xiansong Meng, Xiaowei Guan, Yunhong Ding, and Hao Hu**

Integrated optical phased array (OPA) is evolving into a transformational technology for LiDAR and free-space optical communication systems due to its distinctive qualities of compact size, rapid scanning, and low cost. When the integrated OPA is utilized for long-range vehicle LiDAR (300 m range), a large emission aperture (mm-cm length) is required. However, a large aperture typically necessitates thousands of phase-controlled emitters and consumes tens of watts when utilizing traditional thermo-optic phase shifters. Here, an easy-to-understand theory is proposed and an ultra-sparse aperiodic OPA is experimentally demonstrated with a large aperture (6 mm × 5 mm) using just 120 phase-controlled emitters. In the azimuthal (φ) direction, high resolvable points of ≈ 1300 have attained within a field of view (FOV) beam steering range of 162°. The consumed electric power is only 0.47 W thanks to the ultra-sparse aperiodic spacing (≈50 µm average pitch) and the high-performance optical phase shifters. The fabrication-robust thermo-optic phase shifter achieved high performance in all relevant aspects including power consumption (3.1 mW/π), driving voltage (1.1 V for 2π), insertion loss (0.6 dB), modulation bandwidth (34 kHz), and footprint (42 µm× 42 µm), acting as an ideal phase tuning component in large-scale photonic integrated circuits.

1. Introduction

Optical phased array (OPA), a cutting-edge solid-state beam steering approach, is becoming a viable substitute to mechanical beam steering techniques for light detection and ranging (LiDAR) systems.[1–5] Also, integrated OPAs feature low size, weight, and power (SWaP) and hold great potential for mass production at a low cost. Up to date, integrated OPAs have been realized on a variety of integrated platforms, including silicon (Si),[6–15] silicon nitride (Si_3N_4),[16–18] lithium niobate ($LiNbO_3$),[5,19–21] and indium phosphide (InP).[22] Among these, the silicon platform has the benefit of being fully compatible with the Complementary Metal Oxide Semiconductor (CMOS) production process, thus the silicon OPAs can potentially be monolithically hybrid integrated with the microelectronic circuits.[7,8]

A large number of resolvable points are required for superior object identification over a broad range, which necessitates that the integrated OPA simultaneously have a large field of view (FOV) and a small beam divergence. The number of resolvable points for typical periodic spaced OPA is roughly equivalent to the number of phase-controlled channels N.[23] However, increasing N results in higher power consumption and more intricate electric control circuits.[7] As an alternative, aperiodic sparsely-spaced OPA can produce a high number of resolvable points with significantly reduced phase-controlled channels, greatly decreasing the power consumption and complexity of the controlling circuits.[10,23–25] Especially, in 2021, Taichiro Fukui et al. offered a benchmarking comprehensive theoretical explanation on the aperiodic OPA and experimentally presented the non-redundant OPA to reach a large number of resolvable points.[23] In addition to the reduced channels, energy-efficient thermo-optic (T/O) phase shifters are also essential for further decreasing the power consumption of the OPA.[26]

As a fundamental component of an OPA, the optical phase shifter is crucial to the overall performance of an OPA. The key parameters of an optical phase shifter include power consumption, insertion loss, driving voltage, modulation speed, and footprint. The carrier-depletion electro-optic phase shifter features a large bandwidth and a low power consumption,[27–31] however, the device is typically mm-long with non-negligible insertion loss

H. Qiu, Y. Liu, X. Meng, X. Guan, Y. Ding, H. Hu
DTU Fotonik, Department of Photonics Engineering
Technical University of Denmark
Kgs. Lyngby DK-2800, Denmark
E-mail: huhao@dtu.dk
H. Qiu
Interuniversity Microelectronics Center (IMEC)
Kapeldreef 75, Leuven 3001, Belgium
X. Guan
Jiaxing Key Laboratory of Photonic Sensing & Intelligent Imaging
Jiaxing 314000, China
X. Guan
Intelligent Optics & Photonics Research Center
Jiaxing Research Institute Zhejiang University
Jiaxing 314000, China

The ORCID identification number(s) for the author(s) of this article can be found under https://doi.org/10.1002/lpor.202301177

DOI: 10.1002/lpor.202301177

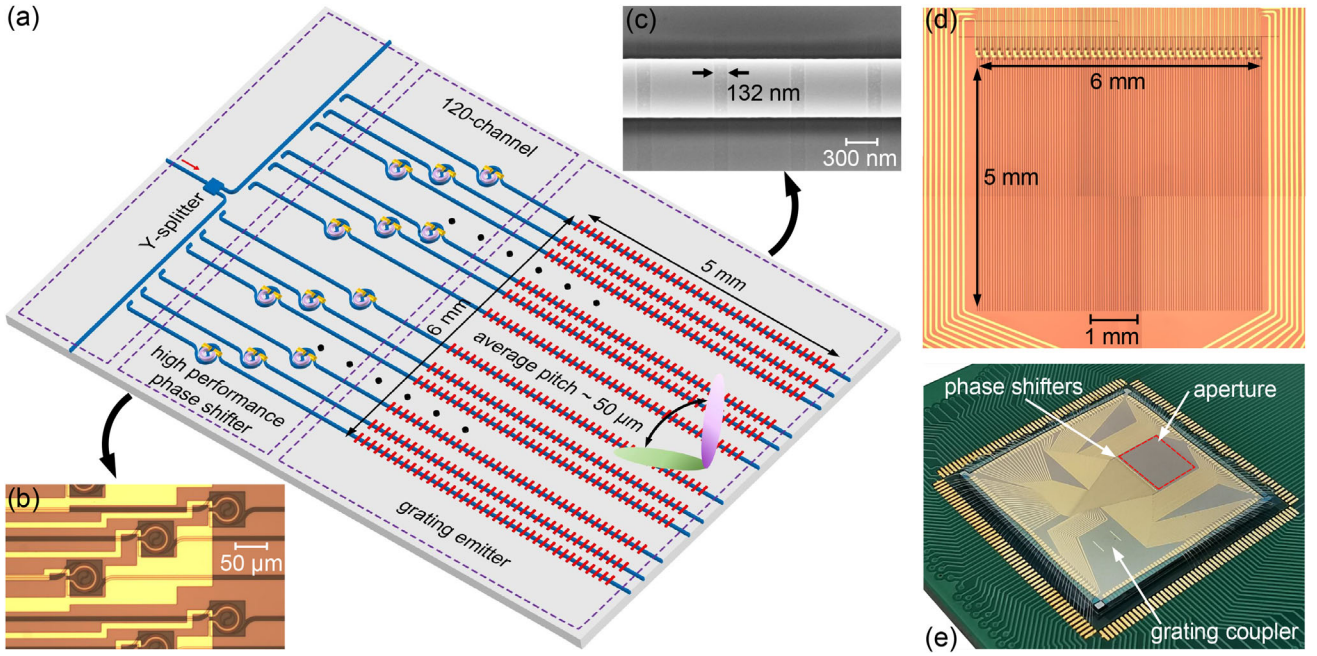

Figure 1. a) Schematic of 120-channel aperiodic OPA. b) Microscope image of the round spiral phase shifter. c) SEM image of the shallow-etched grating emitter. d) Microscope image of aperiodic OPA with the aperture of 6 mm × 5 mm. e) The 2.1 cm × 2.1 cm chip installed on a PCB board.

and the driving voltage is usually incompatible with CMOS microelectronics.

On the other hand, the T/O phase shifter has a simple design, low loss, ease of fabrication, and cost-effectiveness, but it usually consumes a lot of power, which severely restricts its scalability. Although undercutting the silicon substrate can drastically decrease power consumption, it sacrifices the modulation bandwidth. Hence, a small footprint, lower-power, low-loss, and fabrication-robust optical phase shifter with high bandwidth is pivotal for large-scale photonic integration.

Here, we first established the aperiodic OPA theory. We analyzed that the noise in an aperiodic OPA primarily originates from the densely distributed grating lobes, rather than the side lobes located between the grating lobes, and proved that the ultra-sparse aperiodic spacing has little impact on the grating lobe suppression ratio (GLSR, hereinafter referred to as the noise floor). Then we designed a large-aperture (6 mm × 5 mm) OPA with ultra-sparse aperiodic spacing and only 120 phase-controlled channels. We have experimentally achieved high resolvable points of ≈ 1300 (≈ 12000 in simulation) in the phase-controlled direction, limited by the resolution of the experimental setup. To the best of our knowledge, the achieved 162° FOV beam steering range is the largest reported in the experiment so far. The total power consumption is only 0.47 W. The low power consumption benefits from a fabrication-robust T/O round-spiral phase shifter comprising a straightforward width-fixed spiral waveguide along with broad titanium (Ti) heater, which has high performance in all aspects including low power consumption (3.1 mW/π), low insertion loss (0.6 dB), low driving voltage (1.1 V for 2π), high modulation bandwidth (34 kHz) and small footprint (42 μm× 42 μm). The low driving voltage will remarkably reduce the cost of electronic integrated circuits (EIC) by allowing the adoption of low-cost general-purpose CMOS technology.

2. Device Design

2.1. Ultra-Sparse Aperiodic Optical Phased Array

We present a schematic of the 120-channel ultra-sparse aperiodic OPA in **Figure** 1a. Light is coupled into the OPA chip through a vertical grating coupler, and is subsequently distributed to 120 channels through cascaded directional couplers. The round-spiral phase shifter in each channel can be individually controlled to calibrate the OPA and tailor the beam direction. To prevent thermal cross-talk, these phase shifters are staggered with a minimum distance of 107 μm (Figure 1b). The 10-nm shallow etched grating emitter, whose SEM image is illustrated in Figure 1c,[32] emits light into the far field. The ultra-sparse OPA has an average pitch of approximately 50 μm, and the emission aperture is 6 mm × 5 mm, as illustrated in Figure 1d. Figure 1e displays the OPA chip, which is fabricated on the silicon-on-insulator (SOI) platform with the size of 2.1 cm × 2.1 cm and then wire bonded on a printed circuit board (PCB).

2.2. Theoretical Analysis of Ultra-Sparse Aperiodic Spacing

An aperiodic OPA offers the advantage of simultaneously achieving a large FOV and a small beam divergence at the cost of reduced main lobe power, compared with the periodic OPA that has the same number of channels. An ultra-sparse aperiodic OPA can achieve this with a small number of channels, considerably reducing the complexity of wire bonding and electrical control circuits. In contrast, a typical periodic OPA with a half-wavelength pitch ($\lambda/2$) would require thousands of channels to achieve the same aperture and FOV. Moreover, the noise floor in aperiodic OPA shows little variation as the pitch becomes sparser. The theoretical analysis supporting this claim is provided below.

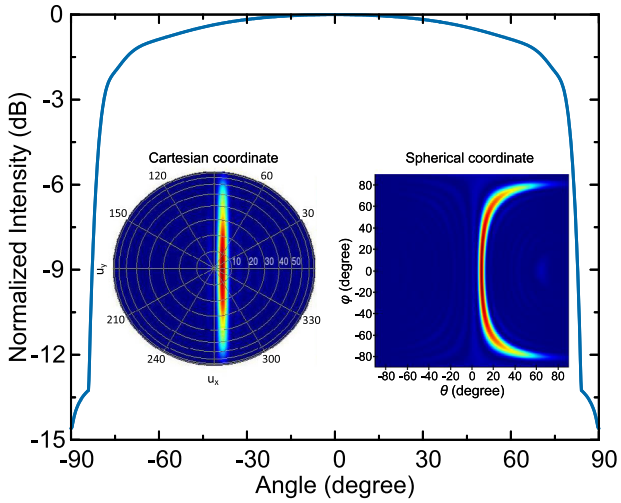

Figure 2. The simulated power cross-section of the element factor for a grating with a width of 0.45 µm. The associated parameters include a pitch of 0.7 µm, a duty cycle of 0.1, and an etch depth of 10 nm. Additionally, the insets display the far-field pattern with Cartesian coordinates and Spherical coordinates for a simulated grating with a length of 10 µm.

The near field and the far field of N-channel aperiodic OPA is described as:

$$e_{near} = ef \otimes af$$
$$E_{far} = \mathcal{F}(ef) \cdot \mathcal{F}(af) = EF_E(\varphi) \cdot AF_E(\varphi) \quad (1)$$

here, e_{near}, ef, and af represent the electric field, element factor, and array factor in the near field, while E_{far}, $EF_E(\varphi)$, and $AF_E(\varphi)$ denote their respective Fourier transforms, representing the electric field, element factor, and array factor in the far field. Notably, the convolution of the near field ef and af results in the product of $EF_E(\varphi)$ and $AF_E(\varphi)$ in the far field. We initiated simulations of the power of the element factor ($|EF_E(\varphi)|^2$) for a grating with a waveguide width of 0.45 µm, matching practical specifications. The practical grating parameters included a pitch of 0.7 µm, an etching duty cycle of 0.1, and an etch depth of 10 nm. Subsequently, we examined the intensity cross-section in the far field and the far-field power pattern with both Cartesian coordinate and Spherical coordinate, as illustrated in **Figure 2**, indicating that the grating is eligible for a large and flat viewable FOV.

While the element factor $EF_E(\varphi)$ does impact the absolute power at different angular positions, it does not affect the noise floor. To analyze these factors, we can disregard the influence of $EF_E(\varphi)$ and instead, concentrate on $AF_E(\varphi)$, which represents the array factor of an aperiodic array, as depicted below:

$$AF_E(\varphi) = \sum_{n=1}^{N} A_n \cdot e^{j\frac{2\pi}{\lambda}x_n \cdot (\sin\varphi - \sin\varphi_0)} \quad (2)$$

In Equation (2), the variable n represents the number of channels, and the A_n signifies the amplitude of the n^{th} emitter. To be able to solve the equation in scalars rather than vectors, we set the origin anywhere but on the same horizontal line as the emitters. Therefore, d_n denotes the aperiodic pitch between the $(n-1)^{th}$ and the n^{th} emitters, $x_n = \sum_1^n d_n$ represents the cumulative distance between the n^{th} emitter and the origin. Furthermore, φ_0 characterizes the inherent emitting angle originating from the original phase of each channel. Then the power distribution of the $AF_P(\varphi) = AF_E(\varphi) \cdot AF_E^*(\varphi)$ can be expressed as follows:

$$AF_P(\varphi) = \sum_{n=1}^{N} A_n^2 + \sum_{n=1}^{N}\sum_{m=1}^{N} 2A_nA_m cos[\frac{2\pi}{\lambda}(x_n - x_m)(\sin\varphi - \sin\varphi_0)]$$
$$(n > m) \quad (3)$$

The far-field power pattern of aperiodic OPA consists of a zero-frequency item and $\frac{N(N-1)}{2}$ interference items. Each interference item represents the beat of any two emitters across all the N emitters. As a result, the multi-beam interference of OPA can be expressed as the power sum of a series of double-beam interference. For each double-beam interference item in Equation (3), similar to Young's interference experiment, each interference item distributes power to multiple angular positions in the far field and generates numerous grating lobes in the far field, and these grating lobes are distributed at the following angular positions:

$$\sin(\varphi_{mn}) - \sin(\varphi_0) = 0, \frac{\lambda}{x_n - x_m}, \frac{2\lambda}{x_n - x_m}, \frac{3\lambda}{x_n - x_m}, \ldots \quad (4)$$

The values of $(x_n - x_m = d_{m+1} + d_{m+2} + \cdots + d_n$ for various m and n are intentionally set as fully random and unequal, causing each interference item in Equation (3) to diffract light into various grating lobes located at different angular positions of φ_{mn}. Consequently, power scatters across space, giving rise to what is commonly referred to as the noise floor of the aperiodic OPA. To distinguish the noise in aperiodic OPA from the noise in periodic OPA, which primarily arises from the side lobes located between two grating lobes rather than the grating lobes themselves, we emphasize the term as the "grating lobe noise". By examining Equation 4, it becomes apparent that each term in Equation (3) contributes to the angular position of φ_0 (highlighted in red as φ_0 in **Figure 3a**), where constructive multi-beam interference occurs among the beams with powers $[\sum_{n=1}^{N} A_n^2 + \sum_{n=1}^{N}\sum_{m=1}^{N} 2A_nA_m \quad (n > m)]$ from the zero-frequency item and all the $\frac{N(N-1)}{2}$ interference items. Consequently, the main lobe exhibits the highest power. However, due to the fully random pitches, i.e., d_1, d_2,..., d_n, the angular solutions in Equation (4) are generally entirely random. In the angular positions of the grating lobe noise floor, only one or a few grating lobe items in Equation (4) contribute to constructive interference, the power for each grating lobe item is $(\sum_{n=1}^{N} A_n^2 + 2A_nA_m)$. Therefore, the power of the noise-grating lobes is significantly lower than that of the main lobe and forms the grating lobe suppression ratio (GLSR), i.e., noise floor. Therefore, the GLSR, i.e., the noise floor is N dependent and almost independent from the value of $x_n - x_m$, which means the sparsity of aperiodic pitch has a negligible effect on the noise floor.

A more intuitive explanation is shown in Figure 3a. Taking the second and the fifth emitters as an example, the beat between them spread the power on angular positions at φ_1, φ_2, φ_0,..., φ_a. Among all of them, the φ_0 represents the main lobe with power P_{25} and all the rest are grating lobes with the power P_{25} as well.

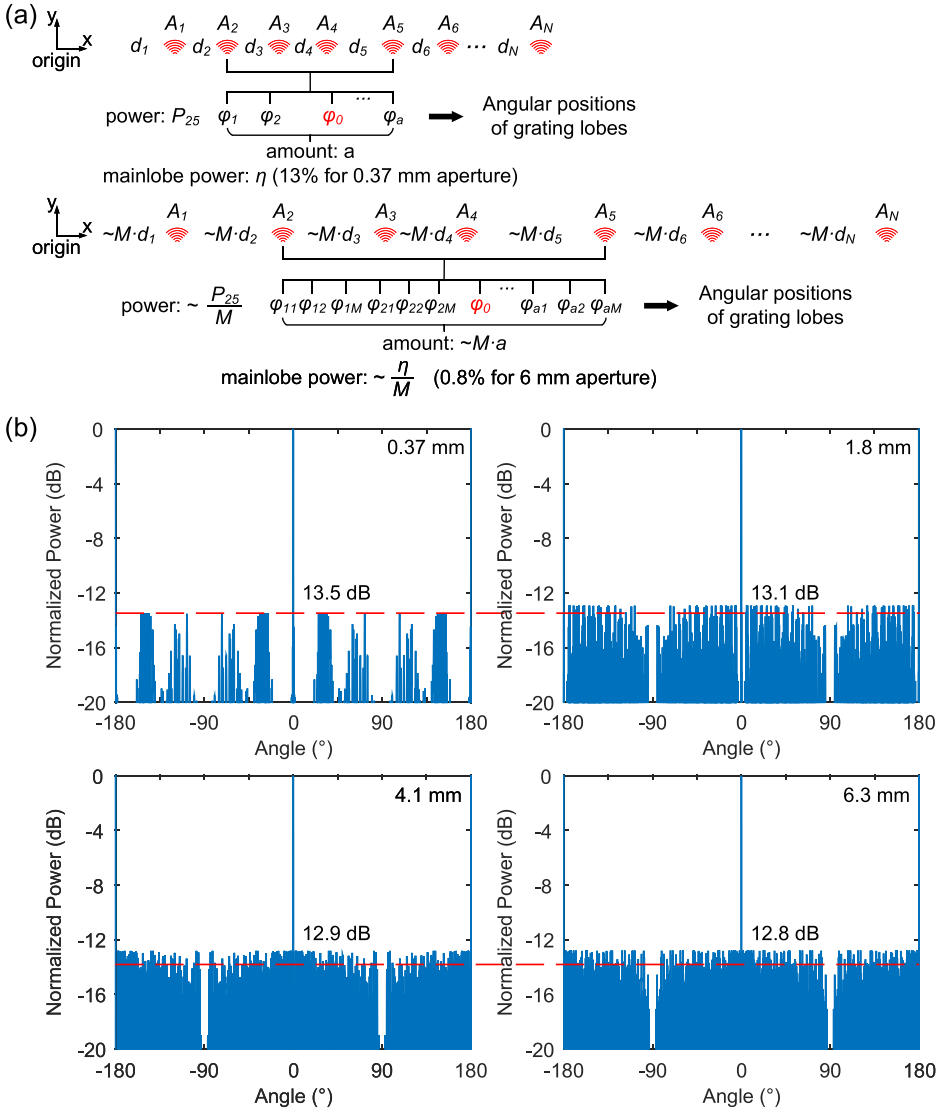

Figure 3. a) Theoretical analysis of ultra-sparse aperiodic spacing. b) Far-field simulation of various apertures with 120 channels. The aperture of (d) is 17 times larger than (a), indicating that sparsity has little effect on the GLSR.

According to Equation (4), when the average pitch of the aperiodic OPA, i.e., the aperture size is scaled up by a factor of M (the pitches will be roughly magnified by M times, shown in Figure 3a), the number of solutions in each term of Equation (4) will increase by a factor of M as well. This implies that there will be M times more "noise grating lobes" in the far field, causing both the power of the main lobe and the "noise grating lobes" to decrease by approximately a factor of M simultaneously, which is illustrated as $\frac{P_{25}}{M}$ in Figure 3a. Consequently, the GLSR remains unaffected. On the other hand, the enlargement of the aperture size results in a decrease in the main lobe power. For instance, the main lobe power is reduced 16.3 times from 13% to 0.8%, almost the same 17 times aperture increase from 0.37 to 6 mm. The power loss from the main lobe is distributed on the added new grating lobes, therefore, even with a 17-times increase in the aperture size, the reduction in main lobe power has a minimal impact on the GLSR. In our simulations, the GLSR experiences a slight decrease from 13.5 to 12.8 dB, as illustrated in Figure 3b. It is worth emphasizing that the pitches in the four images depicted in Figure 3b have not been uniformly scaled by a factor of M, instead, they have been individually optimized, which causes the slight difference in the GLSR ranging from 13.5 to 12.8 dB. As indicated by Equation (4), if the pitches were uniformly scaled by a factor of M, a multitude of new grating lobes would emerge, causing the previously flat noise floor to become irregular. However, it's essential to note that as long as the aperture size and the number of channels remain constant, the number of grating lobes will remain approximately consistent.

We concurrently optimize the power and pitches using the Genetic algorithm. As shown in **Figure** 4a, the GLSR remains

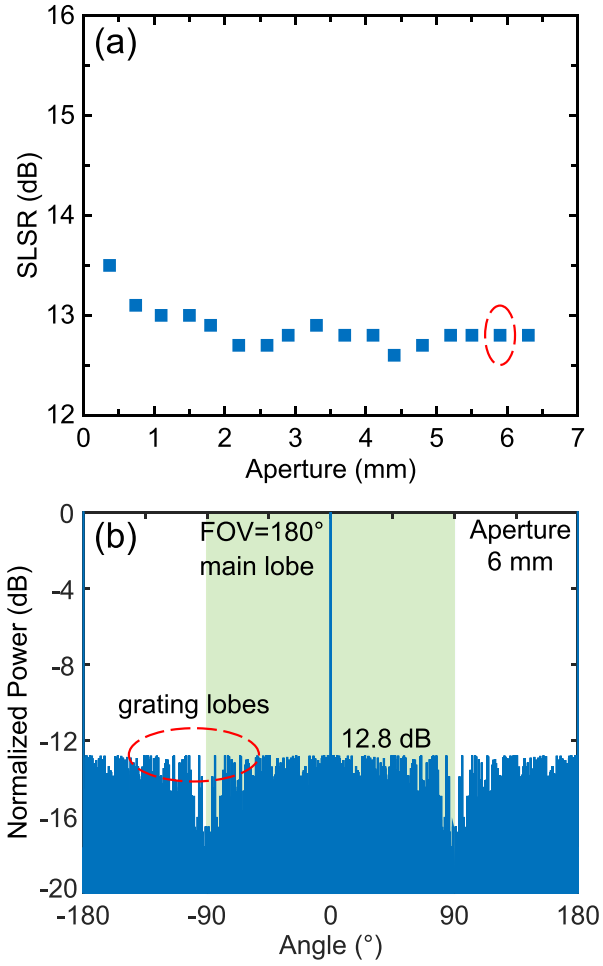

Figure 4. a) Simulated GLSR as a function of the aperture size with fixed 120 channels. c) The simulated far-field figure for a 6 mm aperture, shows an GLSR of 12.8 dB.

almost constant when the aperture size is larger than 2 mm, which agrees well with the theory of aperiodic spacing. Finally, we chose an aperture size of 6 mm with 120 channels, resulting in a GLSR of 12.8 dB. The simulated far field of a 10 μm grating emitter is presented in Figure 4b.

2.3. High-Performance Silicon Round-Spiral Phase Shifter

Our previous research focused on the racetrack-spiral phase shifter, which demonstrated excellent performance across all aspects, as reported in ref. [33]. However, this scheme has a fatal flaw, i.e., its small feature size offset makes it incompatible with the deep ultraviolet (DUV) process. Additionally, the design is complex and susceptible to fabrication errors, making it unsuitable for mass production. As a result, we propose a new structure of round-spiral phase shifter that addresses these drawbacks.

Figure 5a presents a top view of the round-spiral waveguide, which comprises a clockwise (CW) and a counterclockwise (CCW) spiral waveguide that is smoothly connected by a circular S-bend connector with an optimized radius of 5 μm. This radius ensures that the waveguide has a small bend loss and a compact footprint simultaneously. The waveguide radius gradually varies, resulting in a low mode mismatch loss in either the CW or CCW spiral waveguides. We simulated the coupling between the waveguides with various widths w_1 and w_2. Despite the evanescent coupling among all the densely dispersed waveguides,[34] the coupling between the waveguides that are closest to each other dominates. Figure 5b illustrates the coupling model used in our simulation.

The input light is guided into the middle spiral waveguides with a radius of R, and we measure the coupling loss in the neighboring waveguides positioned with a pitch of $\Lambda = 0.9$ μm. The phase-mismatch condition typically requires a significant difference between the widths of the straight waveguides to minimize coupling. However, for sharply bent waveguides, even a small vibration on the radius can have a significant impact on the effective index, leading to minimal coupling loss even when the bend waveguide widths are the same, which represents a significant theoretical improvement over our previous work.[33] Using our model, we simulated and compared the coupling loss among different combinations of waveguide widths. The results are shown in Figure 5c. Strong coupling occurs at $R \approx 12$ μm when the waveguide widths are 450 and 600 nm. However, the simulation shows that the coupling loss remains low when $w_1 = w_2 =$ 500 nm. The purple region in the figure represents the actual radius span of the proposed round-spiral phase shifter. Note that a smaller radius is preferred for a shorter total length of the waveguide with a lower transmission loss. As a result, we designed the proposed phase shifter with a whole waveguide width of 500 nm. This simple structure and design make the work highly replicable for other research groups.

To most efficiently absorb the residual heat, we designed the spiral waveguide with 12 rounds, resulting in a total length of the phase shifter of 1.2 mm. Using Lumerical MODE Solutions, we simulated the total transmission loss of the spiral waveguide with different pitches. The result in **Figure** 6a shows a slight decrease in transmission loss with an increase in pitch. However, a smaller pitch is preferred for a smaller footprint. We found that a pitch of $\Lambda = 0.9$ μm achieves a good balance between low loss and a small footprint. Figure 6b illustrates the light propagation in the spiral waveguide for this pitch.

The full round-spiral T/O phase shifter schematic is shown in **Figure** 7a. In addition to the carefully designed round-spiral waveguide, a Ti-heater is deposited on the SiO_2 layer in the center area of the spiral waveguide. This placement ensures that the residual heat produced by the Ti-heater is maximally absorbed by the densely distributed silicon waveguide, leading to increased energy efficiency. Fabrication of the phase shifter utilizes a standard silicon photonic manufacturing process, and the Ti-heater pattern is defined using UV lithography. The proposed design features a simpler architecture compared with other state-of-the-art T/O phase shifters, such as clothoid bend[35] and multi-pass mode multiplexing.[36] The phase shifter has a small footprint of 42 μm× 42 μm, as shown in the microscope image in Figure 7b.

In general, there are trade-offs among the four main performance aspects of power consumption, insertion loss, modulation speed, and footprint. However, the proposed round-spiral phase

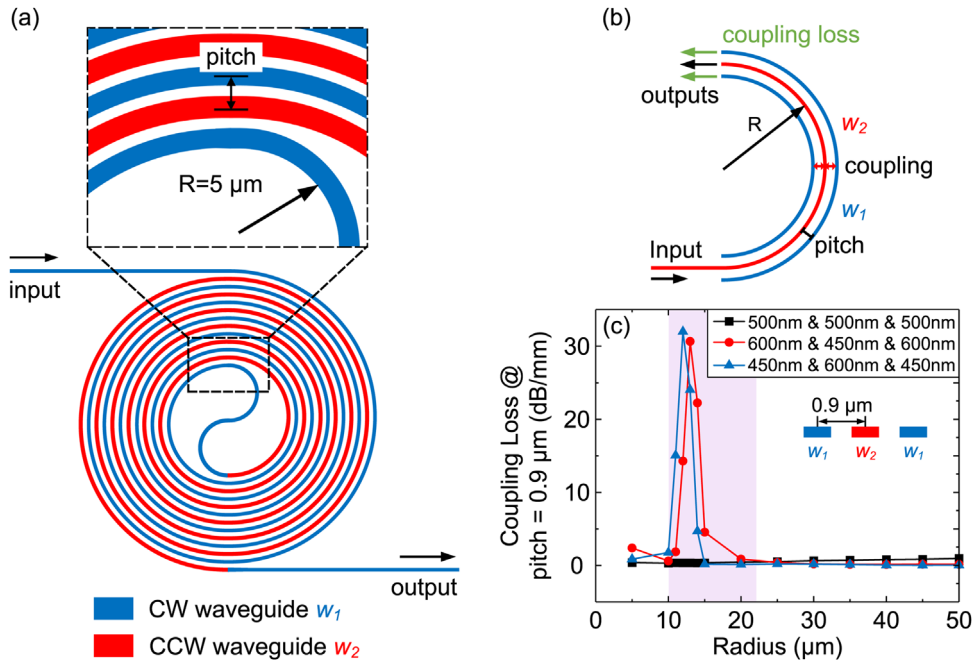

Figure 5. a) Top-view of the round-spiral waveguide, consisting of CW and CCW spiral waveguides with different widths, i.e., w_1 and w_2, and an S-bend connector. The insets indicate that the minimum radius is 5 μm. b) Simulation schematic of the coupling models. c) Coupling loss simulation result comparison. (The purple area is the radius span of the proposed round-spiral phase shifter in practice.).

shifter breaks through these trade-offs and achieves excellent performance in all aspects. Using the cut-back method, the measured insertion loss is only 0.6 dB (Figure 7c), whereas the loss of the straight waveguide (500 nm width) is measured to be 2.7 dBcm^{-1}, providing a benchmark for comparison. The power efficiency was measured in a Mach-Zehnder interferometer (MZI), as shown in Figure 7d. With an increase in electric power from 0 to 6.2 mW, the optical spectrum shifted by a free spectral range (FSR) corresponding to a 2π phase shift. Therefore, the power efficiency is 3.1 mW/π. The driving voltage for the 2π phase shift is as low as 1.1 V, which is fully compatible with low-cost, general-purpose CMOS technologies or Field Programmable Gate Arrays (FPGA) whose output voltage is 3.3 V. In contrast, an electro-optic phase shifter typically requires a high driving voltage or a lengthy structure. The modulation speed was measured as 34 kHz using a 5-kHz square-wave pulse train, as illustrated in Figure 7e. The insets show that the rising time and falling time are 11.6 and 9.2 μs, respectively.

In addition to simple design and deep ultra-violet (DUV) compatibility, the structure is fabrication-robust in many aspects, particularly robust in terms of insertion loss, which remains below 0.8 dB even when w_1 and w_2 vary from 450 to 600 nm, or when Λ varies from 0.9 μm to 1.1 μm. The comparison results are shown in **Figure** 8a,b. In addition, we measured the amplitude vibration induced by the phase modulation, as shown in Figure 8c, by measuring the spontaneous emission spectra from an Erbium-Doped Fiber Amplifier (EDFA) at the output of the phase shifter when applying different electric powers. The negligible ampli-

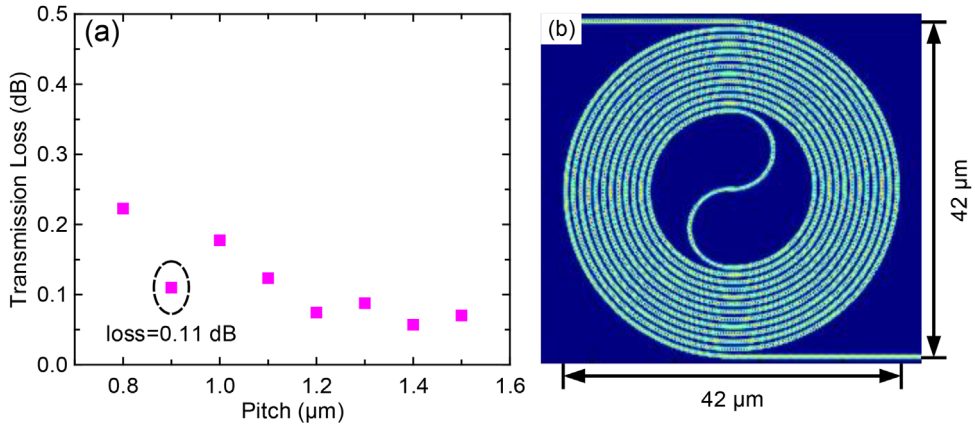

Figure 6. a) Simulated transmission loss of round-spiral phase shifter with pitch varies from 0.8 to 1.5 μm with a step of 0.1 μm. b) Simulated light propagation in the phase shifter for $\Lambda = 0.9$ μm.

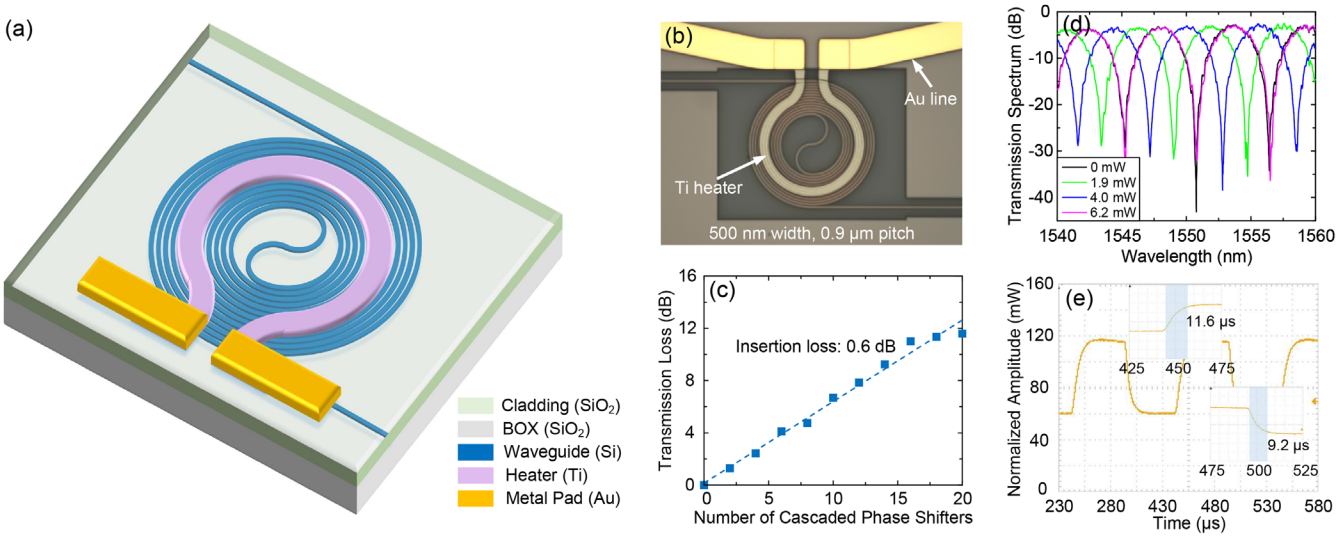

Figure 7. a) Schematic of the high-performance round-spiral phase shifter. b) Microscope image. c) Insertion loss measurement using the cut-back method. d) The power consumption is as low as 3.1 mW/π. e) The measurement of the amplitude modulation induced by phase modulation. f) The measurement of insertion loss over a broad wavelength range.

tude vibration indicates that phase modulation is independent of amplitude modulation, which is a significant advantage over electro-optic modulation, particularly for sensitive devices like OPAs.

We also conducted measurements on the operating bandwidth to the insertion loss. Figure 8d demonstrates that the insertion loss remains stable over a wide bandwidth (1520 to 1580 nm, as limited by our measurement capabilities). The insertion loss per phase shifter was measured as 0.6 ± 0.08 dB, which is crucial for achieving wavelength-reliant 2D beam steering in the OPA Lidar application. Moreover, we observed that the power efficiency of the phase shifter remained nearly constant

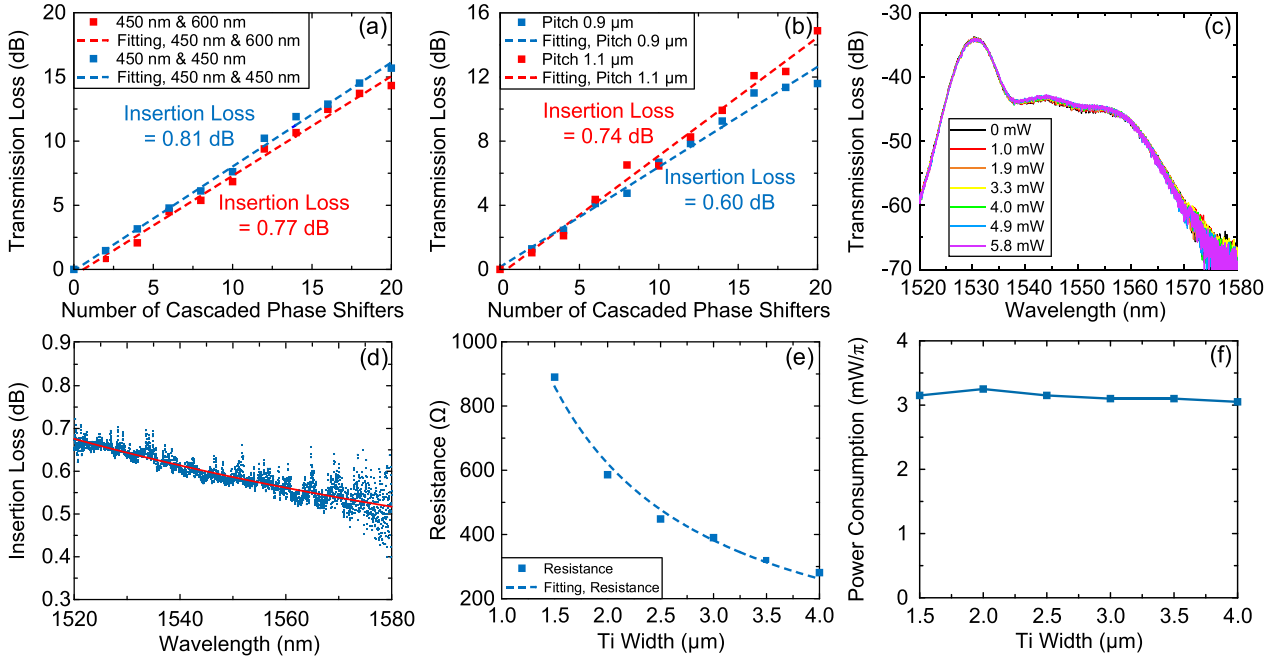

Figure 8. a) The robustness characterization of insertion loss on waveguide widths change. b) The robust characterization of insertion loss on pitch change. c) The negligible measured amplitude modulation induced by phase modulation. d) The robustness characterization of insertion loss over a broad wavelength range. e) The measurement resistance of various Ti-heater widths. f) The robustness characterization of power consumption on various Ti-heater widths.

when the heater width was varied from 1.5 to 4 μm, indicating that the residual heat was effectively absorbed by the spiral waveguide. The measured resistance and power consumption of the Ti-heater with varying widths are illustrated in Figure 8e, f, respectively, demonstrating the robustness of the heater width variation. In summary, due to its superior performance and robustness, the proposed phase shifter is an ideal building block for large-scale photonic integrated circuits, including OPAs, quantum optics,[37] optical neural networks,[38,39] and optical switches.[40]

3. OPA Measurement

Thanks to the low 2π-driving-voltage of 1.1 V, the phase shifter can be conveniently driven by a commercial FPGA. However, the output voltage of the FPGA is fixed at 3.3 V and is not adjustable. To address this issue, we utilized the pulse-width-modulation (PWM) technique to change the output voltage and control the phase shifters.[24,32] To ensure accurate performance, we used the Gradient descent algorithm at a wavelength of 1570 nm to calibrate the phase of each channel, converging the beam at 0° in the φ direction, as shown in **Figure 9**a. After calibrating the beam, we changed the voltage on one specific channel while maintaining the voltages applied to the other channels. As the phase varied from 0 to 2π, the far field power changed following a sin function curve, as depicted in Figure 9b. We achieved a measured energy efficiency of 3.5 mW/π, which is consistent with the individually measured power consumption of the phase shifter, i.e., 3.1 mW/π.

We achieved a large FOV of 162° by steering the beam from -80° to 82°. The normalized far-field powers at each targeted angle are presented in **Figure 10**a, where the measured GLSR ranges from 3 to 6 dB. The discrepancy between the measured and simulated GLSR is attributed to the amplitude vibration of the cascaded directional couplers. In Figure 10b, a zoomed-in image at 0° shows the observed beam divergence, i.e., the resolution in the far field, to be 0.13°. While in the simulation, the beam divergence can reach 0.014° for the designed 6 mm aperture. However, the limited resolution of the camera constraints the observed beam divergence, and the sparse far-field measurement in Figure 10b is one piece of evidence. Another piece of evidence is that the measured beamwidth remains constant over the entire FOV, which does not comply with the theory. Thus, the measurement setup limits the number of resolvable points in the φ direction to 1300, whereas the number of resolvable points can reach approximately 12000 in the simulation.

The laser wavelength can be tuned to steer the beam in the polar (θ) direction with a tuning efficiency of 14.9°/100 nm. By tuning the laser wavelength from 1480 to 1572 nm, a beam steering range of 13.7° was achieved in the θ direction. The corresponding far-field pattern is shown in Figure 10c.

4. Discussion

We have compared the performance of our proposed OPA with that of state-of-the-art OPAs based on T/O phase shifters. Despite

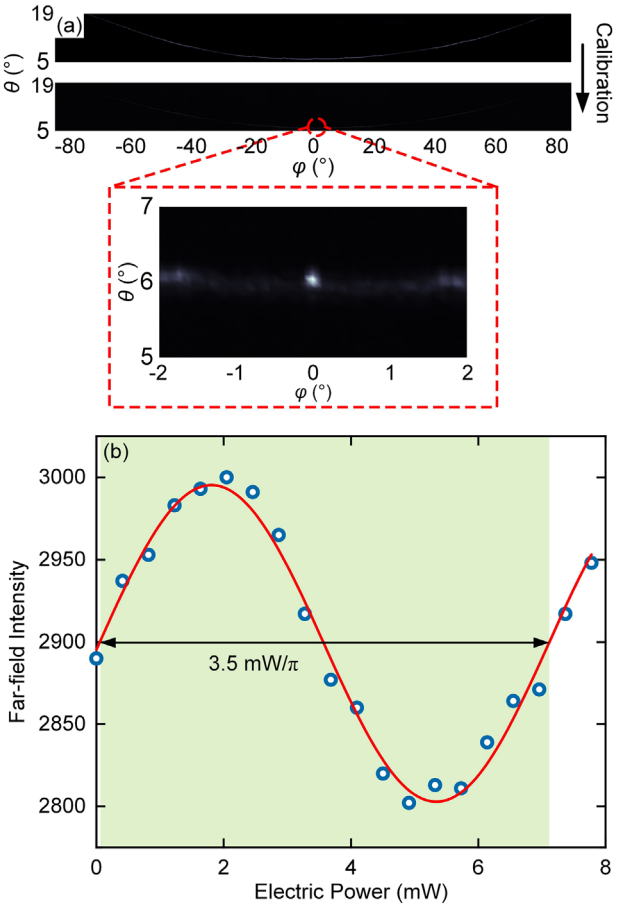

Figure 9. a) Far-field figure before and after calibration. b) Power consumption measurement in a specific channel, showing 3.5 mW/π electrical power usage in OPA.

having only 120 phase-controlled channels, our OPA achieved a large aperture of 6 mm x 5 mm thanks to the ultra-sparse spacing. Furthermore, the overall power consumption of our OPA is only 0.47 W, thanks to the low-power phase shifters used. In our experiment, we were able to measure approximately 1300 resolvable points within a large 162° steering range in the φ direction, as shown in **Figure 11**. Our OPA outperformed other state-of-the-art OPAs in terms of the number of resolvable points achieved per unit power consumption. With an upgraded experimental setup, the resolvable points could be increased up to approximately 12000.

5. Conclusion

We analyze and demonstrate an aperiodic optical phased array with a large aperture (6 mm × 5 mm) only using 120 phase-controlled channels. Within a large beam steering range of 162°, high resolvable points of ≈ 1300 have been achieved in the φ direction. The total consumed electric power is only 0.47 W due to the ultra-sparse aperiodic spacing (≈ 50 μm average pitch) and the high-performance optical phase shifters. The fabrication-

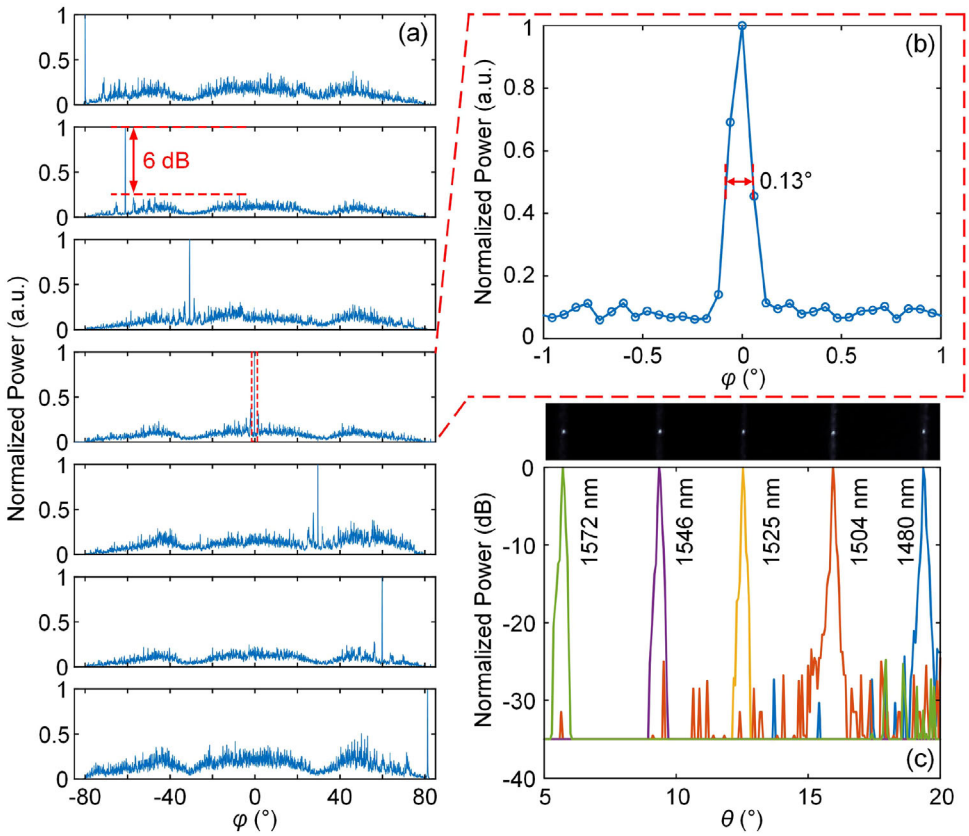

Figure 10. a) -80° to 82° beam steering in the φ direction. b) The zoomed-in figure of (a) at $\varphi = 0°$, shows the measured beam divergence as 0.13° (c) 5.7° to 19.4° beam steering with wavelength tuning in the θ direction.

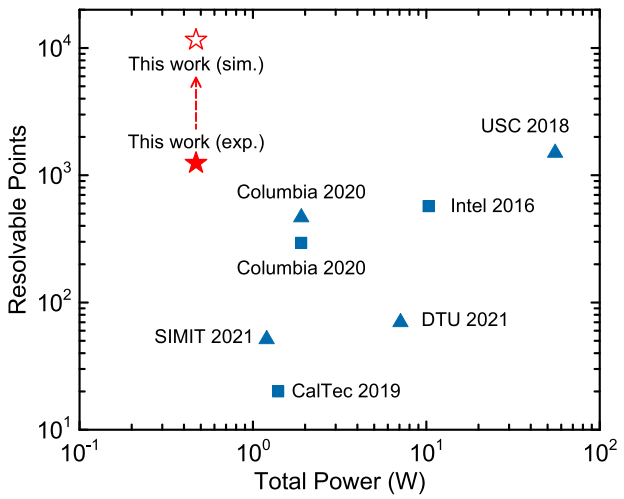

Figure 11. a) Performance comparison among state-of-the-art T/O based OPA.

robust T/O phase shifter achieved superior performance in all relevant aspects including power consumption (3.1 mW/π), driving voltage (1.1 V for 2π), insertion loss (0.6 dB), modulation bandwidth (34 kHz), and footprint (42 μm× 42 μm), representing a desirable phase tuning element for large-scale photonic integrated circuits.

Acknowledgements

The authors would like to acknowledge DTU Nanolab for the support of fabrication facilities and technologies. This work has received financial support from Villum Fonden (15401), Novo Nordisk Fonden (NNF22OC0080333), and the DTU Discovery Grant (96486).

Conflict of Interest

The authors declare no conflict of interest.

Data Availability Statement

The data that support the findings of this study are available from the corresponding author upon reasonable request.

Keywords

lidar, optical phased array, silicon photonics

Received: November 14, 2023
Revised: April 20, 2024
Published online: May 16, 2024

[1] R. T. Collis, *Adv. Geophys.* **1969**, *13*, 113.

[2] D. Wang, C. WatkinsW, H. Xie, *Micromachines* **2020**, *11*, 456.
[3] M. Ryan Halterman, M. Bruch, R. Halterman, *Unmanned Syst. Technol. XII* **2010**, *7692*, 123.
[4] S. Wandel, G. Xu, G. Yang, N. Li, J. Zhang, *IEEE Photon. J.* **2016**, *772*, 012004.
[5] B. Li, Q. Lin, M. Li, *Nature* **2023**, *620*, 316.
[6] J. Sun, E. Timurdogan, A. Yaacobi, E. Shah Hosseini, M. R. Watts, *Nature* **2013**, *493*, 195.
[7] S. Chung, H. Abediasl, H. Hashemi, *IEEE J. Solid-State Circuits* **2018**, *53*, 275.
[8] J. Sun, E. Timurdogan, A. Yaacobi, Z. Su, E. S. Hosseini, D. B. Cole, M. R. Watts, *CLEO: Sci. Innov.* **2020**, *JTh4A*, 3.
[9] Y. Liu, X. Meng, H. Hu, in *CLEO, postdeadline paper*, Optical Society of America, Washington, D.C. **2022**, p. JTh6C.3.
[10] D. N. Hutchison, J. Sun, J. K. Doylend, R. Kumar, J. Heck, W. Kim, C. T. Phare, A. Feshali, H. Rong, *Optica* **2016**, *3*, 887.
[11] Y. Wang, G. Zhou, X. Zhang, K. Kwon, P.-A. Blanche, N. Triesault, K.-s. Yu, M. C. Wu, *Optica* **2019**, *6*, 557.
[12] Z. Xu, Y. Zhou, S. Chen, L. Lu, G. Zhou, J. Chen, L. Zhou, *Frontiers of Optoelectronics* **2021**, *14*, 426.
[13] K. Wang, Y. Wang, X. Guo, Y. Zhang, A. He, Y. Su, *Front. Optoelectron.* **2021**, *14*, 374.
[14] M. Chalupnik, A. Singh, J. Leatham, M. Lončar, M. Soltani, *APL Photonics* **2023**, *8*, 5.
[15] A. Sharma, J. N. Straguzzi, T. Xue, A. Govdeli, F. D. Chen, A. Stalmashonak, W. D. Sacher, J. K. Poon, *Nanophotonics* **2024**.
[16] C.-S. Im, B. Bhandari, K.-P. Lee, S.-M. Kim, M.-C. Oh, S.-S. Lee, *Opt. Express* **2020**, *28*, 3270.
[17] C. Sun, B. Li, W. Shi, J. Lin, N. Ding, H. K. Tsang, A. Zhang, *IEEE J. Sel. Top. Quantum Electron.* **2022**, *28*, 6.
[18] L. Yu, P. Wang, P. Ma, L. Cui, Z. Wang, Y. Yang, Y. Zhang, J. Pan, *J. Lightwave Technol.* **2023**, *41*, 2756.
[19] S. Tan, J. Liu, Y. Liu, H. Li, Q. Lu, W. Guo, *CLEO: Sci. Innov.* **2020**, *SM2M*, 1.
[20] G. Yue, Y. Li, *Opt. Lett.* **2023**, *48*, 3633.
[21] Z. Wang, X. Li, J. Ji, Z. Sun, J. Sun, B. Fang, J. Lu, S. Li, X. Ma, X. Chen, S. Zhu, T. Li, *Nanophotonics* **2024**.
[22] J. Midkiff, K. M. Yoo, J.-D. Shin, H. Dalir, M. H. Teimourpour, R. Chen, *Optica* **2020**, *7*, 1544.
[23] T. Fukui, R. Tanomura, K. Komatsu, D. Yamashita, S. Takahashi, Y. Nakano, T. Tanemura, *Optica* **2021**, *8*, 1350.
[24] R. Fatemi, A. Khachaturian, A. Hajimiri, *IEEE J. Solid-State Circuits* **2019**, *54*, 1200.
[25] D. Lian, S. Zhao, W. Li, J. Chen, D. Dai, Y. Shi, *Nanophotonics* **2024**, *13*, 29.
[26] S. A. Miller, Y.-C. Chang, C. T. Phare, M. C. Shin, M. Zadka, S. P. Roberts, B. Stern, X. Ji, A. Mohanty, O. A. Jimenez Gordillo, U. D. Dave, M. Lipson, *Optica* **2020**, *7*, 3.
[27] Y. Li, B. Chen, Q. Na, Q. Xie, M. Tao, L. Zhang, Z. Zhi, Y. Li, X. Liu, X. Luo, G. Lo, F. Gao, X. Li, J. Song, *Photonics Res.* **2021**, *9*, 2511.
[28] C. V. Poulton, M. J. Byrd, P. Russo, E. Timurdogan, M. Khandaker, D. Vermeulen, M. R. Watts, *IEEE J. Sel. Top. Quantum Electron.* **2019**, *25*, 1.
[29] G. Kang, S.-H. Kim, J.-B. You, D.-S. Lee, H. Yoon, Y.-G. Ha, J.-H. Kim, D.-E. Yoo, D.-W. Lee, C.-H. Youn, K. Yu, H.-H. Park, *IEEE Photonics Technol. Lett.* **2019**, *31*, 1685.
[30] M. Gehl, G. Hoffman, P. Davids, A. Starbuck, C. Dallo, Z. Barber, E. Kadlec, R. K. Mohan, S. Crouch, C. Long, in *2019 Conference on Lasers and Electro-Optics (CLEO)*, IEEE, Piscataway **2019**, pp. 1–2.
[31] W. Tong, E. Yang, Y. Pang, H. Yang, X. Qian, R. Yang, B. Hu, J. Dong, X. Zhang, *Laser Photonics Rev.* **2023**, *17*, 2201032.
[32] H. Qiu, Y. Liu, X. Meng, X. Guan, Y. Ding, H. Hu, *Photonics Res.* **2023**, *11*, 659.
[33] H. Qiu, Y. Liu, C. Luan, D. Kong, X. Guan, Y. Ding, H. Hu, *Opt. Lett.* **2020**, *45*, 4806.
[34] W. Song, R. Gatdula, S. Abbaslou, M. Lu, A. Stein, W. Y. Lai, J. Provine, R. F. W. Pease, D. N. Christodoulides, W. Jiang, *Nat. Commun.* **2015**, *6*, 7027.
[35] S. Chung, M. Nakai, H. Hashemi, *Opt. Express* **2019**, *27*, 13430.
[36] S. A. Miller, Y.-C. Chang, C. T. Phare, M. C. Shin, M. Zadka, S. P. Roberts, B. Stern, X. Ji, A. Mohanty, O. A. J. Gordillo, U. D. Dave, M. Lipson, *Optica* **2020**, *7*, 3.
[37] J. Wang, S. Paesani, Y. Ding, R. Santagati, P. Skrzypczyk, A. Salavrakos, J. Tura, R. Augusiak, L. Mančinska, D. Bacco, D. Bonneau, J. W. Silverstone, Q. Gong, A. Acín, K. Rottwitt, L. K. Oxenløwe, J. L. O'brien, A. Laing, M. G. Thompson, *Science* **2018**, *360*, 285.
[38] N. C. Harris, J. Carolan, D. Bunandar, M. Prabhu, M. Hochberg, T. Baehr-Jones, M. L. Fanto, A. M. Smith, C. C. Tison, P. M. Alsing, D. Englund, *Optica* **2018**, *5*, 1623.
[39] S. Pai, Z. Sun, T. W. Hughes, T. Park, B. Bartlett, I. A. Williamson, M. Minkov, M. Milanizadeh, N. Abebe, F. Morichetti, A. Melloni, S. Fan, O. Solgaard, D. A. B. Miller, *Science* **2023**, *380*, 398.
[40] P. Dumais, D. J. Goodwill, D. Celo, J. Jiang, C. Zhang, F. Zhao, X. Tu, C. Zhang, S. Yan, J. He, M. Li, W. Liu, Y. Wei, D. Geng, H. Mehrvar, E. Bernier, *J. Lightwave Technol.* **2017**, *36*, 233.